








Nonstationarity in the global terrestrial water cycle and its interlinkages in the Anthropocene

Wanshu Nie^{a,b,c,1} , Sujay V. Kumar^a , Augusto Getirana^{a,b}, Long Zhao^d, Melissa L. Wrzesien^{a,e}, Goutam Konapala^f, Shahryar Khaliq Ahmad^{a,b}, Kim A. Locke^{a,b}, Thomas R. Holmes^a , Bryant D. Loomis^g , and Matthew Rodell^{a,h} 

Affiliations are included on p. 10.

Edited by Lan Erlandsson, Stockholms Universitet, Stockholm, Sweden; received February 23, 2024; accepted September 3, 2024 by Editorial Board Member Carl Folke

Climate change and human activities alter the global freshwater cycle, causing nonstationary processes as its distribution shifting over time, yet a comprehensive understanding of these changes remains elusive. Here, we develop a remote sensing–informed terrestrial reanalysis and assess the nonstationarity of and interconnections among global water cycle components from 2003 to 2020. We highlight 20 hotspot regions where terrestrial water storage exhibits strong nonstationarity, impacting 35% of the global population and 45% of the area covered by irrigated agriculture. Emerging long-term trends dominate the most often (48.2%), followed by seasonal shifts (32.8%) and changes in extremes (19%). Notably, in mid-latitudes, this encompasses 34% of Asia and 27% of North America. The patterns of nonstationarity and their dominant types differ across other water cycle components, including precipitation, evapotranspiration, runoff, and gross primary production. These differences also manifest uniquely across hotspot regions, illustrating the intricate ways in which each component responds to climate change and human water management. Our findings emphasize the importance of considering nonstationarity when assessing water cycle information toward the development of strategies for sustainable water resource usage, enhancing resilience to extreme events, and effectively addressing other challenges associated with climate change.

nonstationarity | global water cycle | human disturbance | climate change | data assimilation

Climate change and human activities have altered Earth's natural systems, as evidenced by trends and fluctuations in environmental processes that deviate from historical patterns (1, 2). These shifting patterns and irregularities make it questionable to expect stability when predicting future climate conditions. Reliable understanding of the nature of water cycle change is vital for sustaining water resources, especially for agriculture, the largest consumptive user of fresh water. However, most water resource management activities and associated risk assessments rely on the assumption that the relevant geophysical variables have statistical properties that remain constant over time (1, 3). For example, the frequency and intensity of droughts and floods are often quantified based on the deviations of accumulated precipitation from an assumed, stationary climatology. The nonstationarity of precipitation, therefore, introduces significant uncertainties in the quantification and projection of the severity of hydrological extremes. Beyond meteorological variables such as temperature and precipitation, whose nonstationarity stems from human-induced global warming, terrestrial hydrological processes are directly impacted by human disturbances through activities such as water use, deforestation, urbanization, and damming of rivers, among others. Consequently, the combined influence of climate change and human water management processes is likely to be greater than climate change alone and potentially manifest within a shorter time frame on the terrestrial water cycle, such as increased groundwater pumping during extreme droughts (4), impacting associated stationarity assumptions.

Despite the established research on terrestrial water storage (TWS) trends (5–7), the full extent of nonstationarity in TWS components is poorly understood, as the long-term trend only accounts for part of the nonstationary signal. While changes in variability, the associated changes in extremes, and their link to the existence of a background trend have been extensively studied for atmospheric forcings (8–10), these aspects have received less attention for land hydrological variables in the literature. Recent efforts have been made to separate the contribution of climate variability from the intensification of the water cycle (11–15), to assess the severity of water stress via the trend to variability ratio (16), and to quantify and link water cycle extremes to global warming and other climate indicators (17, 18). However, these studies do not provide a comprehensive analysis of

Significance

Traditional strategies for managing water resources often assume that the probability distribution remains constant over time. However, this is not the case given that climate change and human activities have greatly altered the global water cycle. Our research marks a comprehensive analysis to quantify changes in the global water cycle by considering emerging long-term trends, seasonal shifts, and changes in extreme events. Integrating advanced remote sensing measurements and earth system modeling with innovative analysis methods, we examine how climate variability and human activities have altered the global water cycle over the past two decades. Our findings provide significant insights for enhancing water resource management, infrastructure resilience, and the development of adaptive early warning and monitoring systems.

The authors declare no competing interest.

This article is a PNAS Direct Submission. L.W.E. is a Guest Editor invited by the Editorial Board.

Copyright © 2024 the Author(s). Published by PNAS. This article is distributed under [Creative Commons Attribution-NonCommercial-NoDerivatives License 4.0 \(CC BY-NC-ND\)](https://creativecommons.org/licenses/by-nc-nd/4.0/).

¹To whom correspondence may be addressed. Email: wanshu.nie@nasa.gov.

This article contains supporting information online at <https://www.pnas.org/lookup/suppl/doi:10.1073/pnas.2403707121/-/DCSupplemental>.

Published October 28, 2024.

nonstationarity. In addition, indices used to identify extremes such as droughts based on threshold approaches often assume a fixed seasonal cycle (19–22). This implies that conditions for a specific day, week, or month are ranked based on data from the same calendar dates across different years, without accounting for potential shifts in the timing or shape of seasonality. However, there is now strong evidence linking global warming and human water management to shifts in the seasonal cycles of various water components, ecology, and associated carbon fluxes (23–28). If changing climatology is ignored, the scale used to measure extremes may no longer be appropriate (29–32).

To provide a comprehensive quantification of nonstationarity in terrestrial water cycle, we leverage a state-of-the-art land surface model and multisource remote sensing observations to produce a global analysis at 10 km spatial resolution (*Materials and Methods*). The assimilation of remotely sensed information enhances the realism of hydrological variables in our model, potentially improving detection of the complex interactions between climate variation and human activities on the terrestrial water cycle. A detailed evaluation of the model's performance against reference datasets can be found in *SI Appendix, Supplementary Section 1*. We applied a robust seasonal-trend decomposition algorithm to discretize the time series of water cycle variables into three components: a long-term trend, a seasonal cycle, and a residual. We introduce an innovative nonstationarity index (NSI) based on a global ranking of three metrics: the Theil–Sen slope of the long-term trend time series (TR), the shift in the timing of the seasonal peak based on the seasonal time series (SS), and changes in the frequency of extremes (EFR, accounting for both wet and dry extremes) for places identified with a change point in the residual time series (*Materials and Methods*). NSI ranges from 0 to 1 with larger values of NSI indicating stronger trends, larger seasonal shifts, and greater changes in the frequency of extremes.

Changes in the terrestrial water cycle often manifest more rapidly than typical climatological shifts due to direct human impacts. However, satellite observations capable of detecting these human impacts are primarily available from 2000 onward. Therefore, our quantification of water cycle nonstationarity is defined for the period 2003–2020. To address the challenge of quantifying nonstationarity within a limited time frame and to avoid misidentification of nonstationarity resulting from inherent randomness (3), we ensure that only trends, seasonal shifts, and changes in extremes exceeding predefined thresholds, which we qualify as emerging patterns, are considered for global ranking. These thresholds, which represent the 95% CI for trends, seasonal shifts, and changes in extremes, are derived from constructed stationary scenarios using the corresponding parameter space obtained from the global reanalysis (*Materials and Methods*). Two stationary scenarios (moderate vs. high noise determined by the choice of an autoregressive parameter and the SD of a noise term) are created to test the robustness of the proposed nonstationary approach, and our findings remain consistent regardless of the noise level (*SI Appendix, Supplementary Section 4*).

Results

Nonstationarity in the Water Cycle Across the Globe. Approximately one quarter (23.6%) of the global land surface has undergone strong nonstationary TWS variations over the past two decades (Fig. 1A). About two-thirds of that (62.8%) is in the northern mid-latitudes (N 23.45 to 66.55), including southern North America, the Middle East and North Africa, the northern part of South Asia, and the eastern part of Eurasia. Other regions with high nonstationarity are located in the southern part of South America and central

Australia. We define these “hotspot” areas of nonstationary water cycle changes based on a threshold of NSI greater than 0.5 and identify 20 such regions, as shown in Fig. 1A. More than 80% of the hotspot regions (80.9% of land with NSI > 0.5) overlap with emerging TWS trends ranked in the upper 50th percentile over the globe, with 64% showing a rapid depletion signal associated with human disturbance of water cycle, hydroclimatic extremes, or both (*SI Appendix, Extended Data Figs. 2 and 5*). While the long-term declines in TWS contributing to water cycle nonstationarity in many of the hotspot regions have previously been described (5, 33, 34), it is worth noting that 63% percent of the global total hotspot area also has shifts in seasonal peak timing that exceeds 2 d/yr (equivalent to the median of SS), with 57.8% shifting toward a delayed peak and 42.2% shifting toward an earlier peak (*SI Appendix, Extended Data Fig. 2*). Further, the rate of water cycle extreme event occurrences more than doubled after the identified change point in 43.6% of the hotspot area (*SI Appendix, Extended Data Fig. 2*). In contrast, merely 1.8% of the hotspot area experiences a reduced rate of extreme event occurrences after the change point, with the rate dropping to less than half of the rate before the change occurred (*SI Appendix, Extended Data Fig. 2*).

Nonstationarity in the global water cycle is caused by either the individual or combined impacts of climate change, climate variability, and human water (and land) management. Distinguishing the role of climate from that of human management is often challenging, and the limited time frame further complicates attributing decadal climate variability to nonstationarity. In this context, rather than focusing on the causal relationships between these factors and nonstationarity, we examine multiple related variables together to understand the relative influences of these underlying drivers on a given water cycle process. Here, we group the TWS NSI greater than 0.5 into five bins (G1 to G5) with an interval of 0.1 (Fig. 1E) and display the corresponding NSI distributions for evapotranspiration (ET), runoff, and precipitation based on the same categorization (Fig. 1F–H). Such categorized analysis mitigates the potential misleading effects of pixel-to-pixel interactions, where a signal in one pixel may respond to a variable in another pixel due to factors such as lateral water allocation. While the nonstationarity index of runoff (Fig. 1G), and gross primary production (GPP) (*SI Appendix, Extended Data Fig. 1B*) show a consistent pattern with that of TWS (Fig. 1F and G), regions with the most extensive nonstationarity in TWS do not collocate with those in ET (Fig. 1F). Such disconnects between TWS and vegetation-related fluxes for the G5 category can be largely explained by the mutual effects of TWS decline and irrigated agriculture, in particular, for regions including northwestern India and the North China Plain (*SI Appendix, Extended Data Fig. 5*). The decline of groundwater due to pumping for irrigation inhibits deep soil evaporation due to lowered water tables. On the other hand, such practices stabilize and enhance vegetation productivity and the associated transpiration. The simultaneous observational constraints from remotely sensed soil moisture, TWS, and vegetation improve the simulation of interlinkages among water cycle processes and related human management practices. In northern South America and European Russia, the high NSI values of ET are primarily influenced by either increasing water availability or shifts in seasonality (Figs. 1B and 2B), while that for TWS remains low without major groundwater depletion. The global pattern of NSI in precipitation (Fig. 1D) differs from that of TWS. The nonstationarity for precipitation over these TWS hotspot areas is generally low and has minor differences across bins (Fig. 1H). This limited influence of precipitation nonstationarity provides compelling evidence that human activity drives the nonstationarity patterns of the global terrestrial water cycle. To eliminate the

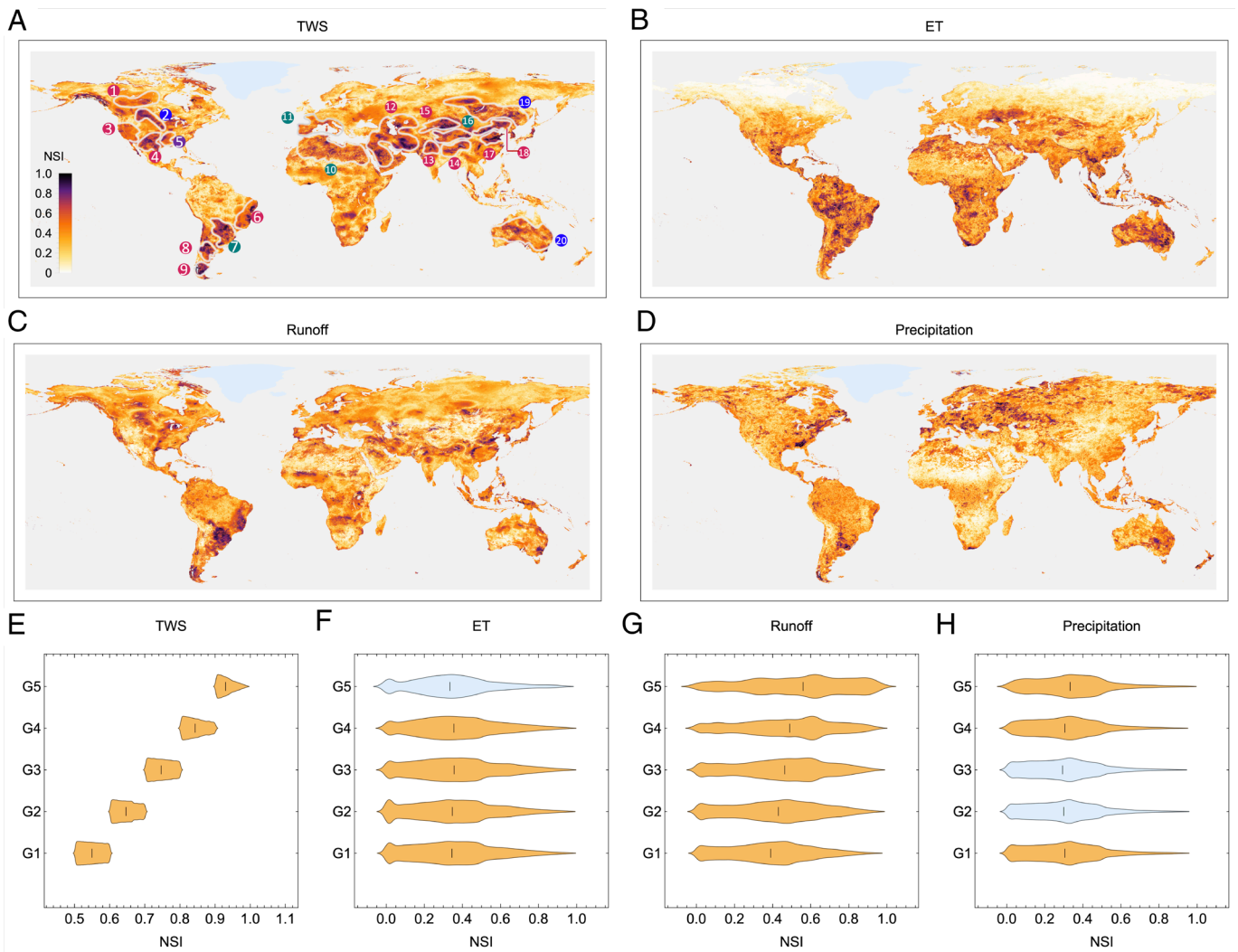


Fig. 1. Global nonstationarity in land water fluxes and precipitation. Global distribution of the integrated nonstationarity index for (A) terrestrial water storage (TWS), (B) evapotranspiration (ET), (C) sum of the surface and subsurface runoff, and (D) precipitation. 20 hotspot regions are highlighted in (A) with the background color of each number indicating the dominant type of nonstationarity for the area and the distribution of the nonstationarity index for TWS for hot spot regions (E) is divided into five subgroups with evenly distributed 10% quantile intervals: G1 (Q50 to Q60), G2 (Q60 to Q70), G3 (Q70 to Q80), G4 (Q80 to Q90), and G5 (Q90 – max). The violin plots (F–H) thus show the distribution of ET, runoff, and precipitation NSI values among the grid cells categorized by the five subgroups. The vertical black line in the violin plot shows the median. The statistical significance ($P < 0.05$; by a one-sided Mann–Whitney U test) of the variable outcome distribution among the subgroups is colored in orange in the violin plot when the variable values within a subgroup of the distribution are significantly greater than the variable values in the adjacent lower subgroups. The violin plots shown in light blue color indicate statistically insignificant distribution difference compared to adjacent lower subgroup. Greenland, Iceland, and glaciers are excluded. The land water fluxes (i.e., TWS, ET, and Runoff) are from the multivariate data assimilation. The precipitation dataset is obtained from the GPM IMERG final version. The nonstationarity index is an average of percentile rank in Theil–Sen–based trend (TR), seasonal shift (SS), and extreme frequency ratio (EFR) associated with the change point. For places where the changing point does not exist, the contribution of EFR is zero. The results for gross primary production (GPP) and precipitation from MERRA2 and ERA5 are shown in [SI Appendix, Extended Data Fig. 1](#) and the metrics that contribute to the NSI calculation (*Materials and Methods*) for all variables are shown in [SI Appendix, Extended Data Figs. 2–4](#).

possibility that the nonstationarity patterns in precipitation are product specific, we calculate the NSI for precipitation based on the ERA5 reanalysis produced by the European Centre for Medium-Range Weather Forecasts (ECWMF) and the version 2 reanalysis of Modern-Era Retrospective Analysis for Research and Applications (MERRA-2) by NASA, in addition to IMERG. We find good agreement in the spatial patterns of NSI ([SI Appendix, Extended Data Fig. 1](#)) between each other.

Attribution of Nonstationarity Patterns in Water Cycle Variables.

Since the NSI provides a comprehensive overview of nonstationary patterns, a detailed analysis of the relative contribution of each component is crucial to pinpoint effectively for specific nonstationary impacts. We investigate the relative contributions of long-term trend, seasonal shift, and extreme frequency ratio to the integrated nonstationarity index (Fig. 2) by computing the metric with the

highest rank percentile among the three components of the NSI, for each grid cell. In this relative rank map, we further distinguish the emerging trends in terms of the sign of the trend (increasing vs. decreasing), direction of the seasonal shift (delayed or advanced), and extreme frequency ratio in terms of whether the extreme occurrences are amplifying ($\text{EFR} > 1$) or reducing ($\text{EFR} < 1$). In Fig. 2, the value and type for each location represent the relatively highest nonstationary measure of the corresponding type ranked from a global perspective.

Globally, long-term trends contribute the most to TWS nonstationarity, occupying 48.2% of the hotspot regions, followed by seasonal shifts and extreme frequency ratios, which cover 32.8% and 19%, respectively (Fig. 2A). Decreasing trends contribute to more than two-thirds of the long-term trend dominated area, ranging from -402 to -3 mm/yr, including well-known hotspot regions such as eastern Brazil (region 6), northwestern India (region 13),

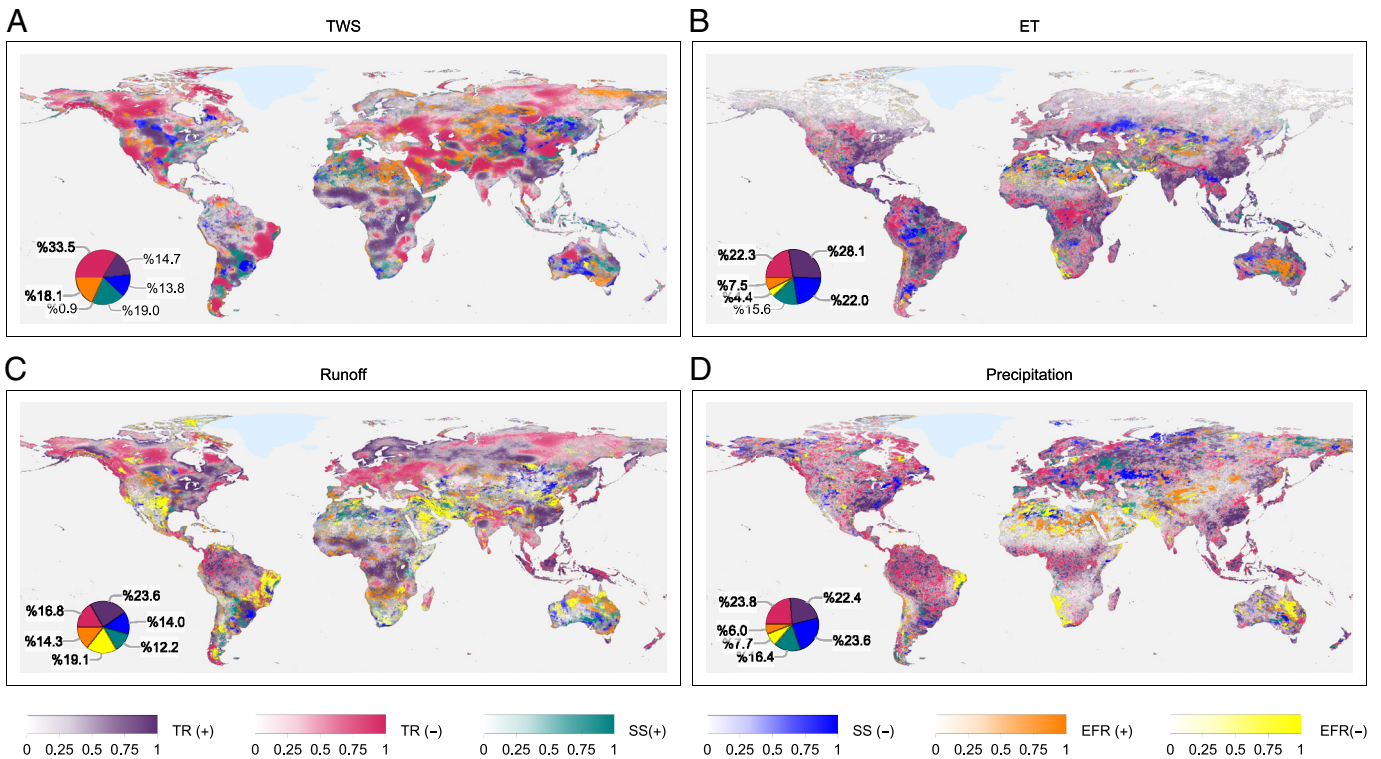


Fig. 2. Dominant type of long-term trend (TR), seasonal shift (SS), and extreme frequency ratio (EFR) to the overall nonstationarity. The color scheme indicates the type and sign of the dominant metric to the overall nonstationarity with the saturation level of the color scheme representing the percentile rank value for the corresponding type. (A–D) shows the dominant type of the nonstationarity metrics for TWS, ET, runoff, and precipitation separately. The pie chart within each subplot summarizes the percent of the land area dominated by each factor out of the total land area where NSI values are greater than 0.5. The results for GPP and precipitation from MERRA2 and ERA5 are shown in *SI Appendix, Extended Data Fig. 7*.

and the North China Plain (region 18) (35–38). Positive trends only contribute to less than one-third of the area, ranging from 3 to 50 mm/yr, such as over the Missouri River Basin (region 2) in the United States. In areas where seasonal shift rank is the dominant constituent of the NSI, 57.9% of the area experiences shifts toward a delayed seasonal peak, including the Pantanal region (region 7), western Africa (region 10), and southwestern Europe (region 11), while 42.1% of the area experience shifts toward an advanced seasonal peak, such as part of Missouri (region 2) and eastern Russia (region 19). The median magnitude of the seasonal shift rate is 4.8 d/year. For the places that dominated by the high rank of extreme frequency ratio, 95% of the area experiences an amplification of extremes after the change point, with the extreme frequency increasing by two to seven times that before the change point. These regions are mostly located in Central and South Asia and the southern part of Australia. Only 5% of the area has experienced a decreasing extreme frequency after the change point.

For TWS, ET, and precipitation, the trend component is the dominant constituent of NSI, followed by seasonal shifts and the extreme frequency ratio (Fig. 2 A, B, and D). Both ET and precipitation are less dominated by changes in extremes, as this type of nonstationarity only occupies less than 15% of its corresponding total hotspot area. For ET and runoff, the positive trends are the primary contributors to nonstationarity over a larger percentage of land. For example, in over 28.1% of the land that experiences high nonstationarity in ET, positive trends are the dominant factor in NSI, whereas negative trends dominate over 22.3% of the area. Similar patterns are also observed for runoff (positive trends over 23.6% and negative trends over 16.8%). For runoff, changes in extremes have a more pronounced impact than seasonal shifts (Fig. 2C), accounting for 33.4% of the land area under high runoff nonstationarity. Within these regions, a greater extent experiences reduced extremes (19.1%)

compared to those with enhanced extremes (14.3%), occurring in the Middle East (region 12), northwestern India (region 13), and the North China Plain (region 18). Over these areas, human-induced aquifer depletion has led to an overall damping of runoff extremes (three examples are provided for the Middle East, North Africa, and South Asia regions in *SI Appendix, Extended Data Fig. 8*), which can be linked to reduced discharge and enhanced infiltration of streamflow to deeper aquifers (31, 39–43).

Hotspots of Water Cycle Nonstationarity. In thirteen of the twenty hotspot regions, the emerging long-term trend was the primary factor in TWS nonstationarity. Twelve regions (regions 1, 3, 4, 6, 8 to 9, 12 to 15, and 17 to 18) have a negative area-averaged TWS trend between -28 mm/yr and -8 mm/yr (Figs. 3, 4). The Lower Mississippi (region 5) is the only region where TWS nonstationarity is dominated by a positive trend at a rate of 3 mm/yr. For these long-term trend-dominated regions, none of them show relatively high nonstationarity in precipitation (averaged NSI > 0.5). In fact, the differences in nonstationarity of TWS and precipitation show that TWS can be strongly nonstationary when precipitation patterns are stationary, particularly over regions that overlap with intensively managed aquifers. For these regions, water assessments based on precipitation data alone would result in the mischaracterization of current and future freshwater availability. For runoff, we observe consistently high nonstationarity across seven regions, with dominant contributions from trends (regions 5, 14), reduced frequency of extreme events (region 6, 9, 17), or a seasonal shift (region 7). This is likely due to the influence of surface water management and groundwater and freshwater consumption, which have impacted the seasonal cycle of river flows and reduced incidences of extremes. The growing pressure on water supplies, along with the increased frequency of dry extremes,

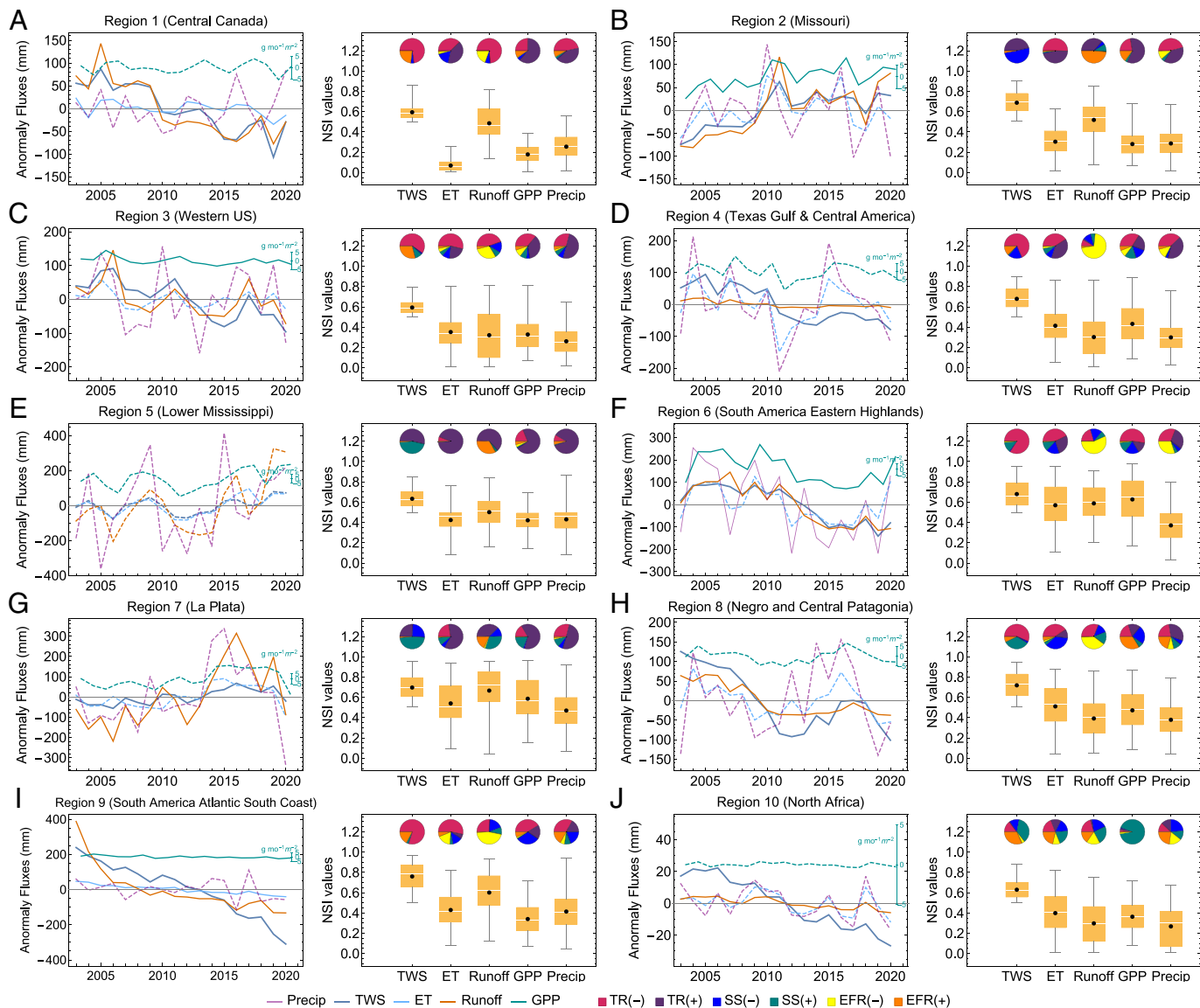


Fig. 3. Changes in fluxes for nonstationary hot spot regions (1–10, subplots A–J) and its relative contributors. Annual anomalies relative to the long-term mean are shown for TWS, ET, runoff, precipitation, and GPP averaged for each region. Solid (dashed) lines indicate statistically significant (insignificant) annual trend according to the Mann–Kendall trend test at 5% significance level. Distribution of nonstationarity index for the five fluxes is shown in boxplots with the black dots indicating the regional mean of NSI, the box boundaries indicating the first (*Lower*) and third (*Upper*) quartile, and the whiskers indicating the 1st (*Lower*) and 99th (*Upper*) percentiles. The pie chart on top of each boxplot summarizes the percent of area maximumly contributed by positive (negative) long-term trend, advanced (delayed) seasonal shift, or intensified (reduced) extreme occurrence.

have been documented to instigate or exacerbate drought- and famine-induced migration, political unrest, and transboundary water conflicts, particularly in the Middle East and North Africa (44–46). While we stop short of recommending approaches for incorporating information on water cycle nonstationarity into water management and policy decisions, we anticipate that locating and classifying areas of significant nonstationarity will increase awareness and facilitate uptake of this information in water management and policy decisions. For all regions dominated by long-term TWS depletion, only eastern Brazil (region 6) is collocated with strong nonstationarity in GPP, dominated by a negative trend, reflecting the combined impacts of deforestation, agricultural intensification, and an extended drought (35, 36, 47). While GPP nonstationarity remains low in most other regions experiencing TWS declines, regions such as the western United States, Eastern and Northern China (regions 3, 17, 18) exhibit predominantly positive trends, indicating greening associated with excessive use of freshwater resources (*SI Appendix, Extended Data*

Fig. 3). Conversely, in the Middle East and Central Asia (regions 12), there is a noticeable shift in GPP seasonality toward a later peak, suggesting a potential alignment with a delayed phenology (48). For Rio Negro and Central Patagonia (region 8) and Indus (region 13), the factors that contribute to nonstationarity in GPP are highly mixed (*SI Appendix, Extended Data Fig. 7*). In these areas, human water management drives the transformation of nonstationary hydrological processes such as greening at the expense of water depletion (see a detailed case study for region 18 in *SI Appendix, Supplementary Section 2*). Consequently, assessments based on vegetation condition would yield results that diverge from those based on water availability if the anthropogenic drivers of nonstationarity are overlooked.

In the remaining seven regions (2, 7, 10, 11, 16, 19, and 20), seasonal shift is the primary influence on TWS nonstationarity (Figs. 3 and 4). For Missouri (region 2), TWS nonstationarity is comparably contributed by seasonal shifts toward an earlier peak (46%) and increasing trends (51%). This is associated with strong

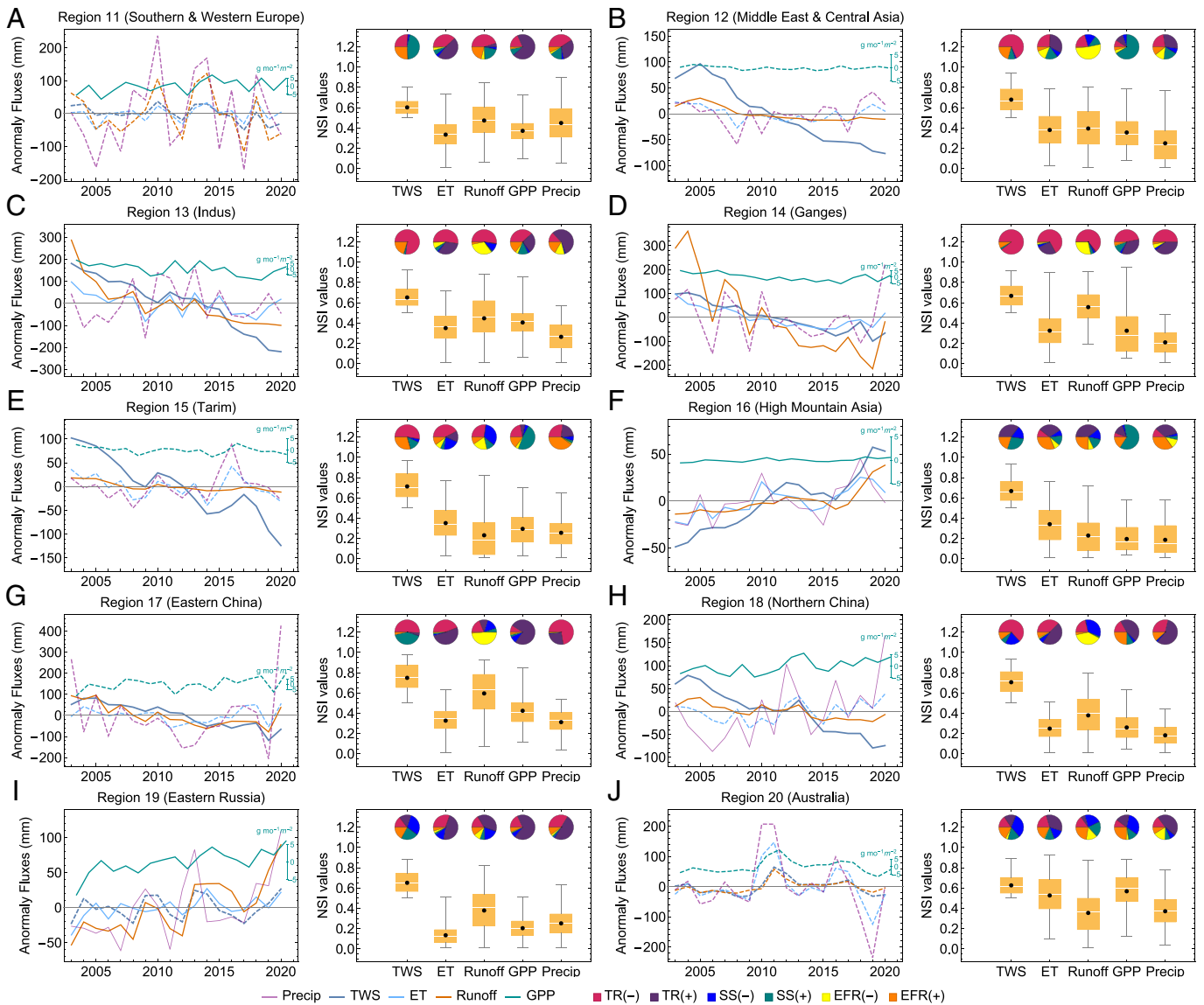


Fig. 4. Continued from Fig. 3 Changes in fluxes for nonstationary hot spot regions (11–20, subplots A–J) and its relative contributors.

nonstationarity in runoff but is dominated by increased extremes. For the La Plata basin (region 7), although TWS nonstationarity is dominated by seasonal shift (73%), the region exhibits an averaged increasing TWS trend, which is associated with increased precipitation. The nonstationarity in GPP is high, with a median NSI value of 0.57. This is predominately due to a greening signal observed across 63% of the region, potentially attributed to land use change and the expansion of crop production (47, 49). North Africa (region 10) exhibits a consistently high prevalence of seasonal shifts across all variables, along with enhanced extreme events, except for GPP, which is primarily driven by a delayed shift in the seasonal peak (92%). In southern and western Europe (region 11), TWS, runoff, and precipitation all show strong nonstationarity. Among them, TWS is dominated by seasonal shifts (46%), while precipitation exhibits mixed trends (72%). Runoff in this region is primarily associated with declining trends (45%) and heightened extremes (21%), which is evidently attributed to the effects of climate change (50). Region 16, covering the inner Tibetan Plateau, has experienced elevated rainfall rates, increased glacier-melt flows, and lake expansions (5, 51). Together, these factors lead to nonstationary TWS, primarily explained by mixed direction in seasonal shifts (45%), followed by positive long-term

trends (35%). The nonstationarity of ET, runoff, and precipitation remains low for this region, but they all show prevalence in positive trends and enhanced extreme events, while changes in GPP are dominated by a seasonal shift toward a delayed peak and positive trends, which are likely contributed by increased warming and wetting climate (52, 53). The hotspot in eastern Russia (region 19) has increased precipitation, ET, runoff, and GPP, while no significant linear trend in TWS has been observed over the study period. Mixed signal in seasonal shifts dominated the TWS nonstationarity for 53% of the area, while both seasonal shifts (25%) and positive trends (55%) contribute to the nonstationarity for runoff. Warming shifts the seasonal cycle of temperature, particularly in the early days of snowmelt, leading to large seasonal shifts in TWS and increased runoff (54). In these regions, climate change is likely a greater contributor to the compounded seasonal shifts in water and carbon fluxes than water or land management. While seasonal shifts currently represent a smaller percentage globally, their prevalence is expected to increase in a warmer future, especially considering the CO₂ fertilization effects on plant phenology and the alterations in rainfall-snowfall partitioning and its impact on snow dynamics (55). Therefore, it is essential to systematically incorporate this type of nonstationarity consideration into the

assessments of extreme events, taking into account regional and elevation-dependent variations. For Australia (region 20), no significant linear trend is identified for any variables on average, yet the mean of the corresponding nonstationarity index of TWS, ET, and GPP fluxes is higher than 0.5. Natural processes changed the timing and magnitude of water cycle variables by up to several years, such as the millennium drought (2001–2009) (56) and the most recent 2017–2019 drought in southeast Australia, amplifying the translation of extreme conditions from the atmosphere to land processes. The nonstationarity of TWS is dominated by a shift toward an earlier peak timing in northeastern Australia (33%), while a delayed peak timing in southwestern Australia (15%). Interestingly, enhanced extreme occurrence only contributes 9% for precipitation while the number is more than doubled when transforming into water and vegetation fluxes. Prolonged drought conditions can shift the seasonality and range of variability of water cycle processes. There are lagged connections between groundwater and other water cycle variables during and following drought that can persist for years. Quantifying these connections and their effects can be challenging and demand further monitoring and investigation in regions such as Australia (57, 58).

Extreme frequency changes are not a primary determinant of the overall TWS nonstationarity in any region. Nonetheless, the contribution from EFR can vary significantly from 1% (for region 5) to 36% (for region 10). Upon investigating the potential relationship between changes in extremes of all variables and the presence of trends in terrestrial water storage, we find that regions with greater TWS trends tend to encompass a greater extent of areas where both TWS and runoff exhibit change points and correspondingly greater changes in extremes. However, the signs of extreme changes (enhancing vs. reducing) differ based on the signs of TWS trends (*SI Appendix, Extended Data Fig. 9 and Supplementary Section 3*). This indicates that changes in water cycle extremes are interconnected and accentuated in the presence of an underlying trend.

Implications and Discussion

Accurate information on changes in freshwater availability, including seasonality and extremes in addition to emerging trends, will be crucial for ensuring food and water security as global warming and human activities shift and disrupt natural processes. Based on our analysis, roughly 35% of the global population (59) and 45% of irrigated land (60) are affected by strong nonstationarity in TWS. Our results are relevant for water resource and infrastructure management efforts and in developing sustainable strategies for early warning and real-time monitoring systems (e.g., floods and droughts). Here, we provide a significant advancement on previous efforts on global water storage depletion and water cycle intensification (5, 15, 16, 61, 62) by explicitly distinguishing and integrating different types of nonstationarity, and examining the interlinkages between water storage and the associated fluxes. These findings are based on the use of the state-of-the-art models and remote sensing observations. Practically, the identification of the hotspot regions highlights areas to focus on for water resource risk assessment and sustainable resource management planning. Furthermore, the results emphasize regional differences on predominant nonstationarity types, which may influence strategies for selecting climatology references for extreme event assessments.

Even though approaches that account for some of the nonstationarity factors have been proposed elsewhere, such as using time-dependent probabilistic distribution (63, 64), moving window climatology (65), and leveraging external covariates (66), these methods, however, are mostly applied to precipitation-based drought indicators, for which the nonstationarity is mostly dependent on

climate patterns with relatively long observational records. However, given that the magnitude and spatial extent of nonstationarity in land surface variables are prominent even within the past two decades, the often used time scale (~ 30 -y climatology) at which nonstationarity is often considered from the atmospheric perspective (67–69) may need to be adjusted and shortened. More importantly, the distribution of nonstationarity differs in water cycle variables because human disturbance has largely altered the response of vegetation to water supply and demand. Regions with strong nonstationarity in water storage may in fact be associated with small long-term changes in precipitation. In such cases, the traditional multivariate drought indicators or integrated drought indicators can no longer provide synchronized or complementary information for places under intensive human water management. Disregarding notions of nonstationarity will result in increased biases in assessments of extremes and inappropriate guidance for operational water resource management.

Accurate knowledge of nonstationary patterns is vital for making more informed projections about future water cycle changes. Wetting and drying tendencies are likely to be amplified under global warming (70), increasing the influence of the climate system in enhancing nonstationarity and complicating human water use in response to these changes. For instance, regions such as the Mediterranean and western North America are already experiencing high nonstationarity and are projected to encounter increased aridity (70). For such regions, consideration of nonstationarity is needed to accurately quantify and distinguish the drivers and impact of drought extremes from aridification. While variability and extremes for precipitation and runoff are projected to increase faster than average changes in most regions of the world according to the IPCC (71), our study found that reduced runoff volume and reduced extremes are less correlated with changes in precipitation, particularly in regions experiencing water storage depletion. Human disturbance of the water cycle may amplify such nonlinear responses. Accurate representation of these processes is essential so that the extent of human impact on both observed and projected water cycle trends is not underestimated (71).

Our research highlights the need to develop a nonstationary framework of relevant variables in land water-energy-carbon cycles so that more realistic assessments of risks to water resource infrastructure at all timescales under climate change and the human context can be developed. Remote sensing-based observations should be integrated into Earth system models as they provide great potential to detect anthropogenic processes and their associated impacts. In the future, with extended remote sensing records for land surface hydrology, it will be possible to better separate the impact of decadal climate variability, climate change, and human (land) water management on nonstationarity. To further facilitate information between Earth system understanding and water management, both land surface hydrological models and atmospheric models need to include the representation of human–water interfaces in operational and reanalysis practices. Understanding the drivers as well as the interlinkages of nonstationarity across water-energy-carbon cycles is essential for optimal representation of the intricate feedback between water availability, carbon uptake, and the rapidly changing climate in integrated assessment systems, allowing for more accurate projections and informed decision-making to strengthen economic livelihoods.

Materials and Methods

Datasets for Data Assimilation. We assimilate remote sensing-based terrestrial water storage, leaf area index (LAI), and surface soil moisture data simultaneously to constrain and correct for the water cycle components, vegetation conditions, and the associated processes.

We use the global TWS anomalies at $0.5^\circ \times 0.5^\circ$ resolution for the period of 2003–2020 provided by the NASA Goddard Space Flight Center (72). Previous studies have shown that assimilating GRACE into global hydrological models or land surface models can improve simulations of the variability and trends of TWS and groundwater and capture the impact of human water management (73–76). These studies also found that the impact of GRACE data assimilation (DA) on snow, runoff, and ET are mixed, partly due to the misrepresentation in model processes (77, 78), requiring either an improvement in model representation of processes that affect the water and energy partitioning (79) or additional constraints for key model states. Here, we employ the latter strategy through the joint assimilation of vegetation and surface soil moisture conditions (80–82) along with TWS.

Assimilating remotely sensed vegetation conditions, such as the leaf area index (LAI), and vegetation optical depth has been shown to improve the estimates of terrestrial carbon fluxes, the associated soil moisture, ET, runoff responses, and the representation of extreme events such as wildfires and droughts (83–85). Here, we use the LAI product at 500 m pixel size and an 8-day interval obtained from the MCD15A2H version 6 Moderate Resolution Imaging Spectroradiometer (MODIS) product (86). The product is reported to properly capture the seasonality of vegetation across most biomes and is able to provide reliable biophysical information in response to climate (87, 88).

For surface soil moisture, we selected the combined active–passive soil moisture dataset developed within the European Space Agency’s Climate Change Initiative (ESA CCI), which is based on four active and twelve passive microwave products and is sampled to a daily scale at 0.25° regular grid (89). The product has been intensively evaluated with in situ observations and has been proven to be useful in a large number of applications (90–92).

All three observations are regridded to the model resolution of 0.1° using the simple bilinear interpolation method prior to data assimilation.

The Noah-MP Land Surface Model. The simulations are conducted using the Noah-MP land surface model (Noah-MP LSM) (93), Version 4.0.1, implemented within the framework of the NASA Land Information System (LIS) (94) (open source software available at <https://github.com/NASA-LIS/LISF>). As an advanced version of the original Noah land surface model (95), Noah-MP offers various parameterization options including surface/groundwater transfer and storage, prognostic vegetation, and frozen soil physics. The enhanced representation of vegetation response to water stress, infiltration and runoff, multilayer snow process has delivered improved performance relative to earlier versions of Noah LSM in the simulation of runoff, soil moisture, snow, and skin temperature in many river basins across the globe (93, 96–98).

Model Configuration. The model is driven by the combination of two meteorological datasets, with the Integrated Multi-satellitE Retrievals for Global Precipitation Measurement (IMERG) (99) final run providing the precipitation data and NASA’s Modern-Era Retrospective Analysis for Research and Applications, version 2 (MERRA-2) (100) providing the remaining dataset of meteorological fields, including 2 m air temperature, 2 m specific humidity, 10 m wind speed, surface pressure, and incoming shortwave and longwave radiation. Both lapse rate and slope-aspect-based topographical corrections are applied to the input meteorology to represent topographic influences on temperature, humidity, pressure, and radiation. The model is applied in offline mode at 0.1° spatial resolution over the global domain for the period of 2003–2020 after a 62-y spin-up. The model is configured using the Moderate Resolution Imaging Spectroradiometer – International Geosphere Biosphere Program (MODIS-IGBP) (101) land cover dataset at 1 km, the machine learning based 250-m soil property and class dataset generated at the International Soil Reference Information Centre (ISRIC) (102), and the Multi-Error-Removed Improved-Terrain (MERIT) (103) elevation at 3-arcsec spatial resolution. The prognostic vegetation module (104) is enabled, along with a Ball-Berry photosynthesis-based stomatal resistance scheme (105–107), to simulate the carbon uptake and allocation among leaf, stem, wood, and root.

Open Loop (OL) and Multivariate Data Assimilation (DA). We first conduct an open loop simulation (OL) for 2003–2020, for which the model runs using the above-mentioned configuration but without assimilating any observations. It serves as a benchmark simulation that enables us 1) provide a baseline to convert the GRACE TWS anomaly observations to TWS prior to data assimilation; and 2) assess the performance of the multivariate data assimilation against reference datasets.

We then jointly assimilate three remote-sensing based observations into the model (DA), including 1) the GRACE mascon TWS anomalies; 2) the gap-filled and interpolated daily LAI retrievals obtained from the MODIS-MCD15A2H Version 6 product; and 3) the combined active and passive ESA CCI soil moisture product.

The GRACE-based TWS anomalies are first converted to TWS by adding an algorithm mean of the OL-based TWS for the baseline period 2004–2009. To assimilate GRACE-based TWS into the model, we use an Ensemble Kalman Smoother (EnKS), as described by Zaitchik et al. (108) and Kumar et al. (74). The ensemble smoother works by generating two iterations. The first iteration generates a model prediction of TWS by averaging daily simulated TWS in the model at the 5th, 15th, and 25th days per month. And the prediction of TWS is then used in the ensemble updates, in which increments are estimated based on the relative uncertainty between GRACE observation and the model ensemble and are added to the TWS averaged across days of the month through the second iteration:

$$X_{T+}^i = X_{T-}^i + K_T(Z_T^i - H_T X_{T-}^i), \quad [1]$$

in which X_{T-}^i and X_{T+}^i are the i th ensemble member of the state vectors before and after the assimilation update, respectively. Z_T^i is the observation vector that is assimilated into the model. H_T is an operator that converts the model states to observation space. The Kalman gain matrix K_T determines the relative weights of uncertainties in the model and the GRACE observations.

The MODIS-based LAI and the ESA CCI soil moisture product are assimilated into the model in both iterations through an Ensemble Kalman Filter (EnKF) (109), with the updates being estimated as indicated in Eq. 1, but at a daily scale whenever an observation that satisfies the corresponding quality control is available.

The uncertainty of the model is estimated from an ensemble of model simulations, developed by applying small perturbations to three meteorological fields (i.e., precipitation (P), incident shortwave (SW), and longwave (LW) radiation), all relevant state variables, and remotely sensed observations that are assimilated into the model. We use an ensemble of 20 members and the ensemble mean output is utilized for all model performance evaluations and nonstationarity assessments. Time series correlations are imposed via a first-order regressive model [AR(1)] with a timescale of 1 d for forcing fields, 3 h for soil moisture, groundwater, and TWS states, 0.5 h for snow water equivalent (SWE), and 1 d for LAI state. Cross-correlations of the perturbations are set within the forcing fields based on known associations between these components (110). It is important to note that the data assimilation system is in general affected by the choice of relative errors between observations and the model, perturbation settings, and the potential nonlinear model response to perturbation and assimilation. Built upon the settings and strategies established by previous studies (83, 111–117), we have performed a number of sensitivity tests while developing the global DA configuration, including testing a range of errors for observations, meteorological forcing, and relevant model state variables. Despite the inherent complexities and potential sources of uncertainties in data assimilation, our chosen settings have consistently demonstrated improved performance in DA compared to OL across water, energy, and carbon fluxes.

Model Performance Evaluation Metric. The model integrations are evaluated using a number of different metrics. As a common evaluation measure, we employ the Mutual Information (MI) metric across all the evaluations. MI is a nonparametric information theory measure to quantify the mutual association between two variables. It does not make assumptions about the statistical properties of the variables and considers both the individual probabilities of each variable and the joint probabilities of both variables occurring together. Larger MI values imply a stronger relationship between the two variables, while a lower score indicates less dependence. The MI metric is calculated as

$$MI(M: O) = \sum_{\min M} \sum_{\min O} p(M, O)(m, o) \cdot \log \left(\frac{p(M, O)(m, o)}{p_M(m)p_O(o)} \right), \quad [2]$$

where M and O represent model and observations, respectively, p_M and p_O are the marginal probability density functions, and $p(M, O)$ is the joint probability functions.

We also employ Root Mean Square Error (RMSE) to highlight the errors in magnitudes of the estimates in the comparison of the runoff and GPP fields.

$$RMSE = \sqrt{\sum_{i=1}^N \frac{(M_i - O_i)^2}{N}}, \quad [3]$$

where M_i and O_i are the model and observation values, respectively, \bar{O} represents the mean observation value, and N represents the total number of model-observation pairs.

Details of all reference datasets used for evaluation and the corresponding evaluation results are provided in *SI Appendix, Supplementary Section 1*, and considering the overall superior performance of DA over the OL simulation, we then focus only on the DA-based output for the nonstationarity assessment.

Robust STL and Nonstationarity Metrics. We apply a robust seasons-trend decomposition algorithm (RobustSTL) (118) to time series of target variables to extract the long-term trend, seasonal, and the subseasonal to interannual signals. Compared to the classical and widely used Loess decomposition method (119), the RobustSTL method is capable of detecting abrupt changes in trend and residual as well as seasonal fluctuations and shifts. The noise is removed using a local bilateral filter and the trend component is estimated by solving regression using the least absolute deviation loss, both of which decrease the sensitivity to outliers. Additionally, RobustSTL decomposition does not assume Gaussian distributions, as the loss function involves the summation of absolute errors instead of square errors, the later being associated with Gaussian distributions. Before applying the RobustSTL method, we normalize a given time series at the weekly scale (X) into the range of 0 to 1 (X^s) using the min-max linear scaling algorithm so that the same set of parameters can be applied across spatial locations for one variable and among different variables. Then the RobustSTL method is used to decompose X^s into three components:

$$X^s = X_{long}^s + X_{seas}^s + X_{rem}^s, \quad [4]$$

where X_{long}^s is the trend in time series, and X_{seas}^s is the seasonal signal with period T_i , which is set to 52 (wk) for this study. X_{rem}^s denotes the remainder signal, which includes subseasonal and interannual variabilities.

To assess the nonstationarity of a given variable, we consider the long-term trend, seasonal shifts, and changes in the frequency of extremes associated with a change point. The long-term trend (TR) is estimated as the Theil-Sen slope (120) of the X_{long}^s component multiplied by the min-max scaling factor to convert the slope back into its original magnitude. We use the Theil-Sen slope instead of the standard linear slope as the Theil-Sen slope reflects the median of the slopes through pairs of points, which ensures that the resulting trend is less sensitive to large anomalies and outliers.

The seasonal shift (SS) is a measure of the trend in the timing of seasonal peaks during the study period, with negative values indicating a shift toward an earlier peak and positive values indicating a shift toward a later peak. We adapted the approach from Wasko et al. (121) to compute SS . We first identify the timing of the seasonal minimum (t_{min}^i) for each calendar year i in X_{seas}^s component. We then apply circular statistics to project t_{min}^i to an angular value as

$$\theta_{min}^i = \frac{t_{min}^i}{L_i} \cdot 2\pi, \quad [5]$$

where L_i is the number of weeks for year i .

The mean direction $\bar{\theta}_{min}^i$ is then calculated by

$$\bar{\theta}_{min}^i = \begin{cases} \tan^{-1}\left(\frac{S}{C}\right) & S \geq 0, C > 0 \\ \tan^{-1}\left(\frac{S}{C}\right) + \pi & C \leq 0 \\ \tan^{-1}\left(\frac{S}{C}\right) + 2\pi & S < 0, C > 0 \end{cases}, \quad [6]$$

where $C = \sum_{i=1}^n \cos\theta_{min}^i$ and $S = \sum_{i=1}^n \sin\theta_{min}^i$. The water year is defined locally at each grid cell as the 12-month period beginning in the month of $\bar{\theta}_{min}^i$. We

then identify the timing of seasonal peak (t_p^i) for each local water year i in X_{seas}^s component. We also project t_p^i to the angle of circumference by

$$\theta_p^i = \frac{t_p^i}{L_i} \cdot 2\pi. \quad [7]$$

Seasonal shift under the projected coordinate (SS_θ) is then estimated as the Theil-Sen slope of the projected seasonal peaks.

The final SS is estimated by converting SS_θ into the unit of days as

$$SS = \frac{365}{2\pi} (SS_\theta)^{0.5}. \quad [8]$$

Besides the long-term trend and seasonal shifts, the changing climate, along with human intervention, may cause abrupt shifts in the mean and the variability of the states beyond the deterministic patterns, leading to changes in the occurrence of extreme events. We quantify this aspect of nonstationarity by first detecting whether there is a change point associated with the frequency of extreme events and then estimating the ratio of extreme frequencies (EFR) before and after the detected change point.

We first normalize X_{rem}^s by using the standard score statistics:

$$Z_{X_{rem}^s} = \frac{X_{rem,i}^s - \mu_{X_{rem}^s}}{\sigma_{X_{rem}^s}}, \quad [9]$$

where $z_{X_{rem}^s}$ is the normalized value for time step i , and $\mu_{X_{rem}^s}$ and $\sigma_{X_{rem}^s}$ are the mean and SD of X_{rem}^s , respectively. To minimize the impact of outliers on the detection of the change point, we converted the $z_{X_{rem}^s}$ time series into a binary time series to represent extreme events and nonextreme events using the criteria of the absolute value of standard score falling below or above 1. That said, both dry and wet extreme events are considered together:

$$BinaryTS(z_{X_{rem}^s}) = \begin{cases} 0, & \text{if } |z_{X_{rem}^s}| \leq 1 \\ 1, & \text{if } |z_{X_{rem}^s}| > 1 \end{cases}. \quad [10]$$

We then apply a binary segmentation single change point detection algorithm to divide $BinaryTS(z_{X_{rem}^s})$ into two parts, and EFR is estimated as the ratio of the frequency of extreme events during the period before and after the change point:

$$EFR = \frac{\sum_{i=L-L_1+1}^L BinaryTS(z_{X_{rem}^s})}{L-L_1} \cdot \frac{L_1}{\sum_{i=1}^{L_1} BinaryTS(z_{X_{rem}^s})}, \quad [11]$$

where L is the length of the time series, and L_1 is the length of time period before the change point. The binary segmentation method is robust due to its sequential approach that identifies the most pronounced change point and its robustness in accommodating various statistical tests and penalty functions. By converting the time series to a binary format, it effectively reduces sensitivity to outliers, making it particularly suitable for detecting significant frequency changes and abrupt human-induced disruptions. However, it is important to note that this binary approach may be less effective in detecting gradual changes, such as those associated with meteorological extremes.

An EFR greater than 1 indicates that the occurrence of the extreme events during the period after the change point is greater than the period before the change point, implying an intensification of the extreme events. Conversely, an EFR less than 1 implies a reduction in extreme events after the change point. Areas that have not been detected with a change point are masked out from the analysis. Additionally, locations where a change point is detected in the first or last four years are also excluded. We select this threshold for two primary reasons: 1) from a climate perspective, a time scale less than five years may not sufficiently represent the variability in extremes; and 2) low sample density may negatively affect the robustness of frequency analysis. A flowchart of the data processing and the calculation of the nonstationarity metrics and the integrated index is complemented by *SI Appendix, Extended Data Fig. 6*.

The Integrated Nonstationarity Index (NSI). We compute a metric, the integrated nonstationarity index, by integrating the information on the trend, seasonal shift, and extreme frequency ratio as follows:

$$NSI = \frac{PR_{TR} + PR_{SS} + PR_{EFR}}{3}, \quad [12]$$

where PR_{TR} , PR_{SS} , and PR_{EFR} are the percentile of the absolute value of TR , SS , and the absolute value of natural logarithm of EFR ranked within its own context over the globe, respectively, all ranging from 0 to 1.

Since nonstationary behavior can also exist in stationary time series due to random causes (3), especially given a short time record, we adopt threshold-based constraints to truncate the global cumulative distribution of each metric before applying the percentile ranking, so that places with trends, seasonal shifts, or changes in extremes lower than their corresponding threshold are not considered nonstationary.

The threshold-based constraints are derived based on the constructed stationary scenarios with their statistical properties drawn from the parameter space of the corresponding variable in the global reanalysis data.

First, we construct stationary time series by combining a stationary seasonal component, a random Gaussian noise, with an autoregression process of order 1 [AR(1)] as follows:

$$X_t = \phi X_{t-1} + \text{Sin}(2\pi ft) + \varepsilon_t(0, \sigma), \quad [13]$$

where ϕ is the autoregressive parameter with higher values indicating a stronger positive autocorrelation, approximating the strength of the memory of the water cycle components. The SD of the noise term (σ) determines the relative signal of noise to the seasonal amplitude, which is drawn from the extremes to variability ratio (hereinafter parameter space) estimated as the mean absolute deviation of X_{rem}^s divided by the mean absolute deviation X_{seas}^s for the corresponding variable.

A moderate- and a high-constraint stationary scenario is generated to test the robustness of the proposed nonstationary approach. The moderate constraint sets ϕ and σ to 0.5 and the median of the parameter space, while the high-constraint sets ϕ and σ to 0.9 and the upper quartile of the parameter space, respectively. Each stationary scenario consists of 10,000 simulations to ensure statistical robustness. The RobustSTL algorithm is then applied to the time series in the constructed stationary scenarios to acquire the trend, seasonal shift, and changes in extreme metrics. Values at the 95% CI for each metric are then used as threshold values to truncate the cumulative distribution of the corresponding metric of the global reanalysis data prior to percentile ranking. The main text presents results derived from moderate constraints, while a comparative analysis between the outcomes of moderate and high constraints can be found in *SI Appendix, Supplementary Section 4*.

The truncated global cumulative distribution of each metric is binned into 100 equal bins with a percentile interval of 0.01. The percentile rank for each metric for a given location is then estimated based on the binned cumulative distribution. The natural logarithm of the EFR is used before estimating the percentile ranks, as the nonstationarity of an extreme frequency decline by X times is considered equivalent to that of an extreme frequency increase by X times. For instance, an extreme frequency ratio of 0.5 indicates that the frequency of the occurrence of extreme events after the change point has been reduced by half when compared

to the period before the change point. The percentile rank of this EFR is equal to the percentile rank of an EFR of 2, which indicates the frequency of the occurrence of extreme events after the change point has been doubled when compared to the period before the change point.

By definition, NSI ranges from 0 to 1. An NSI value of 0 indicates no trend, no shifted seasonality, and no changes in extreme frequency before and after the change point, while an NSI value of 1 indicates the strongest trend (either positive or negative), largest seasonal shifts (either positive or negative), and strongest changes in extreme frequency (either enhanced or reduced). Note that glaciers, Iceland, and Greenland have been masked out from the analysis due to the model's limitations in representing the relevant processes in such areas. The glacier mask is created based on the glacier database from Global Land Ice Measurements from Space (GLIMS) (122). For places where the change point detection is marked as invalid, PR_{EFR} does not exist and NSI consists only is the average of PR_{TR} and PR_{SS} .

We also examine the relative contribution, or relative importance, of the three types of metrics to the nonstationarity of the target variables. We display a predominant nonstationarity type map with each grid marked with a metric determined by the maximum among PR_{TR} , PR_{SS} , and PR_{EFR} and the intensity shows the percentile rank of the corresponding metric (Fig. 2). We also distinguish the sign of TR , SS , and the logarithm of EFR . 20 hotspot regions with high NSI values are identified to analyze the composition of the nonstationary variation as well as the relationship among the three. Region-averaged time series after scaling with its long-term mean for TWS, ET, runoff, precipitation, and GPP are calculated to provide a comprehensive view of nonstationarity in the water budget and the potential interactions with vegetation growth. Note that the analysis on inter-linkages among key variables does not focus on analyzing causal relationships between nonstationarity in TWS and other variables, given limitations in the observational coverage and limited understanding of underlying processes and mechanisms. Instead, we leverage the best available observational constraints via data assimilation and use a "convergence of evidence" approach across multiple variables to make inferences on attributions.

Data, Materials, and Software Availability. NetCDF, DAT, and CSV data have been deposited in Johns Hopkins Research Data Depository (<https://doi.org/10.7281/T1/KOTDPY>) (123).

ACKNOWLEDGMENTS. The research was supported by the NASA-sponsored Earth Information Science (EIS) pilot project. Computational resources were provided by the NASA's Center for Climate Simulation (NCCS).

Author affiliations: ^aHydrological Sciences Lab, National Aeronautics and Space Administration (NASA) Goddard Space Flight Center, Greenbelt, MD 20771; ^bScience Applications International Corporation, McLean, VA 22102; ^cDepartment of Earth and Planetary Sciences, Johns Hopkins University, Baltimore, MD 21218; ^dDepartment of Analytics and Operations, National University of Singapore, Queenstown, Singapore 119245; ^eEarth System Science Interdisciplinary Center, University of Maryland, College Park, MD 20740; ^fPacific Northwest National Laboratory, Richland, WA 99354; ^gGeodesy and Geophysics Laboratory, NASA Goddard Space Flight Center, Greenbelt, MD 20771; and ^hEarth Sciences Division, NASA Goddard Space Flight Center, Greenbelt, MD 20771

Author contributions: W.N., S.V.K., and A.G. designed research; W.N. and S.V.K. performed research; B.D.L. contributed data; W.N., S.V.K., L.Z., M.L.W., G.K., S.K.A., B.D.L., and M.R. analyzed data; and W.N., S.V.K., A.G., L.Z., G.K., S.K.A., K.A.L., T.R.H., and M.R. wrote the paper.

1. P. C. Milly *et al.*, Stationarity is dead: Whither water management? *Science* **319**, 573–574 (2008).
2. G. E. Galloway, If stationarity is dead, what do we do now? *JAWRA J. Am. Water Resour. Assoc.* **47**, 563–570 (2011).
3. L. J. Slater *et al.*, Nonstationary weather and water extremes: A review of methods for their detection, attribution, and management. *Hydrol. Earth Syst. Sci.* **25**, 3897–3935 (2021).
4. P.-W. Liu *et al.*, Groundwater depletion in California's Central Valley accelerates during megadrought. *Nat. Commun.* **13**, 7825 (2022).
5. M. Rodell *et al.*, Emerging trends in global freshwater availability. *Nature* **557**, 651–659 (2018).
6. B. R. Scanlon *et al.*, Global models underestimate large decadal declining and rising water storage trends relative to GRACE satellite data. *Proc. Natl. Acad. Sci. U.S.A.* **115**, E1080–E1089 (2018).
7. V. Humphrey, L. Gudmundsson, S. I. Seneviratne, Assessing global water storage variability from GRACE: Trends, seasonal cycle, subseasonal anomalies and extremes. *Surv. Geophys.* **37**, 357–395 (2016).
8. S. I. Seneviratne *et al.*, "Weather and climate extreme events in a changing climate" in *Climate Change 2021: The Physical Science Basis. Contribution of Working Group I to the Sixth Assessment Report of the Intergovernmental Panel on Climate Change* V. Masson-Delmotte *et al.* eds.

- (Cambridge University Press, Cambridge, United Kingdom and New York, NY, USA, 2021), pp. 1513–1766, 10.1017/9781009157896.013.
9. N. Nicholls *et al.*, Changes in climate extremes and their impacts on the natural physical environment. *Manag. Risks Extreme Events Disasters Adv. Clim. Change Adapt.* 109–230 (2012).
10. Q. Sun *et al.*, A global, continental, and regional analysis of changes in extreme precipitation. *J. Clim.* **34**, 243–258 (2021).
11. S.-K. Min, X. Zhang, F. W. Zwiers, G. C. Hegerl, Human contribution to more-intense precipitation extremes. *Nature* **470**, 378–381 (2011).
12. X. Zhang *et al.*, Attributing intensification of precipitation extremes to human influence. *Geophys. Res. Lett.* **40**, 5252–5257 (2013).
13. S. Paik *et al.*, Determining the anthropogenic greenhouse gas contribution to the observed intensification of extreme precipitation. *Geophys. Res. Lett.* **47**, e2019GL086875 (2020).
14. L. Gudmundsson *et al.*, Globally observed trends in mean and extreme river flow attributed to climate change. *Science* **371**, 1159–1162 (2021).
15. A. Eicker *et al.*, Does GRACE see the terrestrial water cycle "intensifying"? *J. Geophys. Res. Atmos.* **121**, 733–745 (2016).

16. B. D. Vishwakarma *et al.*, Re-assessing global water storage trends from GRACE time series. *Environ. Res. Lett.* **16**, 034005 (2021).
17. M. Rodell, B. Li, Changing intensity of hydroclimatic extreme events revealed by GRACE and GRACE-FO. *Nat. Water* **1**, 241–248 (2023).
18. J. Kusche *et al.*, Mapping probabilities of extreme continental water storage changes from space gravimetry. *Geophys. Res. Lett.* **43**, 8026–8034 (2016).
19. M. Svoboda *et al.*, The drought monitor. *Bull. Am. Meteorol. Soc.* **83**, 1181–1190 (2002).
20. M. C. Anderson *et al.*, An intercomparison of drought indicators based on thermal remote sensing and NLDAS-2 simulations with US Drought Monitor classifications. *J. Hydrometeorol.* **14**, 1035–1056 (2013).
21. J. A. Keyantash, J. A. Dracup, An aggregate drought index: Assessing drought severity based on fluctuations in the hydrologic cycle and surface water storage. *Water Resour. Res.* **40** (2004).
22. K. C. Mo, Model-based drought indices over the United States. *J. Hydrometeorol.* **9**, 1212–1230 (2008).
23. H. W. Linderholm, Growing season changes in the last century. *Agric. For. Meteorol.* **137**, 1–14 (2006).
24. J. S. Clark, J. Melillo, J. Mohan, C. Salk, The seasonal timing of warming that controls onset of the growing season. *Glob. Change Biol.* **20**, 1136–1145 (2014).
25. I. T. Stewart, Changes in snowpack and snowmelt runoff for key mountain regions. *Hydrol. Process.* **23**, 78–94 (2009).
26. T. P. Barnett, J. C. Adam, D. P. Lettenmaier, Potential impacts of a warming climate on water availability in snow-dominated regions. *Nature* **438**, 303–309 (2005).
27. Y. Pokhrel *et al.*, Global terrestrial water storage and drought severity under climate change. *Nat. Clim. Change* **11**, 226–233 (2021).
28. W. R. Berghuijs, R. A. Woods, M. Hrachowitz, A precipitation shift from snow towards rain leads to a decrease in streamflow. *Nat. Clim. Change* **4**, 583–586 (2014).
29. I. T. Stewart, D. R. Cayan, M. D. Dettinger, Changes in snowmelt runoff timing in western North America under a business as usual climate change scenario. *Clim. Change* **62**, 217–232 (2004).
30. K. N. Musselman *et al.*, Slower snowmelt in a warmer world. *Nat. Clim. Change* **7**, 214–219 (2017).
31. I. E. M. de Graaf *et al.*, Environmental flow limits to global groundwater pumping. *Nature* **574**, 90–94 (2019).
32. A. Getirana *et al.*, Avert Bangladesh's looming water crisis through open science and better data. *Nature* **610**, 626–629 (2022).
33. A. Asoka, T. Gleeson, Y. Wada, V. Mishra, Relative contribution of monsoon precipitation and pumping to changes in groundwater storage in India. *Nat. Geosci.* **10**, 109–117 (2017).
34. B. R. Scanlon *et al.*, Groundwater depletion and sustainability of irrigation in the US High Plains and Central Valley. *Proc. Natl. Acad. Sci. U.S.A.* **109**, 9320–9325 (2012).
35. A. Getirana, Extreme water deficit in Brazil detected from space. *J. Hydrometeorol.* **17**, 591–599 (2016).
36. A. Getirana, R. Libonati, M. Cataldi, Brazil is in water crisis—it needs a drought plan. *Nature* **600**, 218–220 (2021).
37. M. Rodell, I. Velicogna, J. S. Famiglietti, Satellite-based estimates of groundwater depletion in India. *Nature* **460**, 999–1002 (2009).
38. Z. Huang *et al.*, Subregional-scale groundwater depletion detected by GRACE for both shallow and deep aquifers in North China Plain. *Geophys. Res. Lett.* **42**, 1791–1799 (2015).
39. T. Gleeson, M. Cuthbert, G. Ferguson, D. Perrone, Global groundwater sustainability, resources, and systems in the Anthropocene. *Annu. Rev. Earth Planet. Sci.* **48**, 431–463 (2020).
40. S. Jasechko *et al.*, Widespread potential loss of streamflow into underlying aquifers across the USA. *Nature* **591**, 391–395 (2021).
41. A. Mukherjee, S. N. Bhanja, Y. Wada, Groundwater depletion causing reduction of baseflow triggering Ganges river summer drying. *Sci. Rep.* **8**, 12049 (2018).
42. N. Abou Zaki *et al.*, Evaluating impacts of irrigation and drought on river, groundwater and a terminal wetland in the Zayanderud Basin, Iran. *Water* **12**, 1302 (2020).
43. V. B. Chagas, P. L. Chaffe, G. Blöschl, Climate and land management accelerate the Brazilian water cycle. *Nat. Commun.* **13**, 5136 (2022).
44. P. H. Gleick, M. Shimabuku, Water-related conflicts: Definitions, data, and trends from the water conflict chronology. *Environ. Res. Lett.* **18**, 034022 (2023).
45. L. Eklund *et al.*, Societal drought vulnerability and the Syrian climate-conflict nexus are better explained by agriculture than meteorology. *Commun. Earth Environ.* **3**, 85 (2022).
46. L. Bertassello *et al.*, Food demand displaced by global refugee migration influences water use in already water stressed countries. *Nat. Commun.* **14**, 2706 (2023).
47. C. Chen *et al.*, China and India lead in greening of the world through land-use management. *Nat. Sustain.* **2**, 122–129 (2019).
48. L. Wu *et al.*, Impacts of climate change on vegetation phenology and net primary productivity in arid Central Asia. *Sci. Total Environ.* **796**, 149055 (2021).
49. S. A. Abou Rafee *et al.*, Hydrologic response to large-scale land use and cover changes in the Upper Paraná River Basin between 1985 and 2015. *Reg. Environ. Change* **21**, 1–14 (2021).
50. L. Gudmundsson *et al.*, Observed trends in global indicators of mean and extreme streamflow. *Geophys. Res. Lett.* **46**, 756–766 (2019).
51. X. Li *et al.*, Climate change threatens terrestrial water storage over the Tibetan Plateau. *Nat. Clim. Change* **12**, 801–807 (2022).
52. Z. Zhu *et al.*, Greening of the Earth and its drivers. *Nat. Clim. Change* **6**, 791–795 (2016).
53. H. Teng *et al.*, Climate change-induced greening on the Tibetan Plateau modulated by mountainous characteristics. *Environ. Res. Lett.* **16**, 064064 (2021).
54. P. Groisman *et al.*, Dryland belt of Northern Eurasia: Contemporary environmental changes and their consequences. *Environ. Res. Lett.* **13**, 115008 (2018).
55. L. S. Huning, A. AghaKouchak, Global snow drought hot spots and characteristics. *Proc. Natl. Acad. Sci. U.S.A.* **117**, 19753–19759 (2020).
56. A. I. van Dijk *et al.*, The Millennium Drought in southeast Australia (2001–2009): Natural and human causes and implications for water resources, ecosystems, economy, and society. *Water Resour. Res.* **49**, 1040–1057 (2013).
57. K. Fowler *et al.*, Explaining changes in rainfall-runoff relationships during and after Australia's Millennium Drought: A community perspective. *Hydrol. Earth Syst. Sci.* **26**, 6073–6120 (2022).
58. T. J. Peterson, M. Saft, M. C. Peel, A. John, Watersheds may not recover from drought. *Science* **372**, 745–749 (2021).
59. E. Doxide-Whitfield *et al.*, Taking advantage of the improved availability of census data: A first look at the gridded population of the world, version 4. *Pap. Appl. Geogr.* **1**, 226–234 (2015).
60. J. M. Salmon *et al.*, Global rain-fed, irrigated, and paddy croplands: A new high resolution map derived from remote sensing, crop inventories and climate data. *Int. J. Appl. Earth Obs. Geoinf.* **38**, 321–334 (2015).
61. B. D. Hamlington, J. T. Reager, H. Chandanpurkar, K. Y. Kim, Amplitude modulation of seasonal variability in terrestrial water storage. *Geophys. Res. Lett.* **46**, 4404–4412 (2019).
62. L. Jensen *et al.*, Long-term wetting and drying trends in land water storage derived from GRACE and CMIP5 models. *J. Geophys. Res. Atmos.* **124**, 9808–9823 (2019).
63. Y. Wang, J. Li, P. Feng, R. Hu, A time-dependent drought index for non-stationary precipitation series. *Water Resour. Manage.* **29**, 5631–5647 (2015).
64. S. Russo *et al.*, Projection of occurrence of extreme dry-wet years and seasons in Europe with stationary and nonstationary Standardized Precipitation Indices. *J. Geophys. Res. Atmos.* **118**, 7628–7639 (2013).
65. A. Cancelliere, G. D. Mauro, B. Bonaccorso, G. Rossi, Drought forecasting using the Standardized Precipitation Index. *Water Resour. Manage.* **21**, 801–819 (2007).
66. J. Z. Li, Y. X. Wang, S. F. Li, R. Hu, A nonstationary Standardized Precipitation Index incorporating climate indices as covariates. *J. Geophys. Res. Atmos.* **120**, 12082–12095 (2015).
67. A. Arguez *et al.*, NOAA's 1981–2010 US climate normals: An overview. *Bull. Am. Meteorol. Soc.* **93**, 1687–1697 (2012).
68. A. Arguez, R. S. Vose, The definition of the standard WMO climate normal: The key to deriving alternative climate normals. *Bull. Am. Meteorol. Soc.* **92**, 699–704 (2011).
69. Z. H. Hoylman, R. K. Bocsinsky, K. G. Jencso, Drought assessment has been outpaced by climate change: Empirical arguments for a paradigm shift. *Nat. Commun.* **13**, 2715 (2022).
70. Intergovernmental Panel on Climate Change, "Water cycle changes" in *Climate Change 2021–The Physical Science Basis: Working Group I Contribution to the Sixth Assessment Report of the Intergovernmental Panel on Climate Change*, (Cambridge University Press, Cambridge, 2023), pp. 1055–1210.
71. Intergovernmental Panel on Climate Change, "Weather and climate extreme events in a changing climate" in *Climate Change 2021–The Physical Science Basis: Working Group I Contribution to the Sixth Assessment Report of the Intergovernmental Panel on Climate Change*, (Cambridge University Press, Cambridge, 2023), pp. 1513–1766.
72. B. D. Loomis, S. B. Luthcke, T. J. Sabaka, Regularization and error characterization of GRACE mascons. *J. Geod.* **93**, 1381–1398 (2019).
73. M. Grotto, G. J. De Lannoy, R. H. Reichle, M. Rodell, Assimilation of gridded terrestrial water storage observations from GRACE into a land surface model. *Water Resour. Res.* **52**, 4164–4183 (2016).
74. S. V. Kumar *et al.*, Assimilation of gridded GRACE terrestrial water storage estimates in the North American Land Data Assimilation System. *J. Hydrometeorol.* **17**, 1951–1972 (2016).
75. S. Tian *et al.*, Improved water balance component estimates through joint assimilation of GRACE water storage and SMOS soil moisture retrievals. *Water Resour. Res.* **53**, 1820–1840 (2017).
76. B. Li *et al.*, Global GRACE data assimilation for groundwater and drought monitoring: Advances and challenges. *Water Resour. Res.* **55**, 7564–7586 (2019).
77. B. A. Forman, R. H. Reichle, M. Rodell, Assimilation of terrestrial water storage from GRACE in a snow-dominated basin. *Water Resour. Res.* **48** (2012).
78. M. Grotto *et al.*, Benefits and pitfalls of GRACE data assimilation: A case study of terrestrial water storage depletion in India. *Geophys. Res. Lett.* **44**, 4107–4115 (2017).
79. W. Nie *et al.*, Assimilating GRACE into a land surface model in the presence of an irrigation-induced groundwater trend. *Water Resour. Res.* **55**, 11274–11294 (2019).
80. N. Tangdamrongsub *et al.*, Multivariate data assimilation of GRACE, SMOS, SMAP measurements for improved regional soil moisture and groundwater storage estimates. *Adv. Water Resour.* **135**, 103477 (2019).
81. T. Xu *et al.*, Improve the performance of the Noah-MP-Crop model by jointly assimilating soil moisture and vegetation phenology data. *J. Adv. Model. Earth Syst.* **13**, e2020MS002394 (2021).
82. B. Bonan *et al.*, An ensemble square root filter for the joint assimilation of surface soil moisture and leaf area index within the Land data assimilation system LDAS-Monde: Application over the euro-mediterranean region. *Hydrol. Earth Syst. Sci.* **24**, 325–347 (2020).
83. S. V. Kumar *et al.*, Assimilation of remotely sensed leaf area index into the Noah-MP land surface model: Impacts on water and carbon fluxes and states over the continental United States. *J. Hydrometeorol.* **20**, 1359–1377 (2019).
84. D. M. Mocko, S. V. Kumar, C. D. Peters-Lidard, S. Wang, Assimilation of vegetation conditions improves the representation of drought over agricultural areas. *J. Hydrometeorol.* **22**, 1085–1098 (2021).
85. S. V. Kumar *et al.*, The 2019–2020 Australian drought and bushfires altered the partitioning of hydrological fluxes. *Geophys. Res. Lett.* **48**, e2020GL014111 (2021).
86. R. Myneni, Y. Knyazikhin, T. Park, MCD15A2H MODIS/Terra+Aqua leaf area index/FPAR 8-day L4 global 500m SIN grid V006. NASA USGS. 10.5067/MODIS/MCD15A2H.006. Accessed 4 March 2022.
87. K. Yan *et al.*, Evaluation of MODIS LAI/FPAR product collection 6. Part 1: Consistency and improvements. *Remote Sens.* **8**, 359 (2016).
88. K. Yan *et al.*, Evaluation of MODIS LAI/FPAR product collection 6. Part 2: Validation and intercomparison. *Remote Sens.* **8**, 460 (2016).
89. W. Dorigo *et al.*, ESA CCI soil moisture for improved Earth system understanding: State-of-the-art and future directions. *Remote Sens. Environ.* **203**, 185–215 (2017).
90. A. Gruber *et al.*, Evolution of the ESA CCI soil moisture climate data records and their underlying merging methodology. *Earth Syst. Sci. Data* **11**, 717–739 (2019).
91. J. Ikonen *et al.*, The Sodankylä in situ soil moisture observation network: An example application of ESA CCI soil moisture product evaluation. *Geosci. Instrum. Methods Data Syst.* **5**, 95–108 (2016).
92. A. Al-Yaari *et al.*, Assessment and inter-comparison of recently developed/reprocessed microwave satellite soil moisture products using ISMN ground-based measurements. *Remote Sens. Environ.* **224**, 289–303 (2019).
93. G. Y. Niu *et al.*, The community Noah land surface model with multiparameterization options (Noah-MP): 1. Model description and evaluation with local-scale measurements. *J. Geophys. Res.* **116**, 1381–19 (2011).
94. S. V. Kumar *et al.*, Land information system: An interoperable framework for high resolution land surface modeling. *Environ. Model. Softw.* **21**, 1402–1415 (2006).
95. M. B. Ek *et al.*, Implementation of Noah land surface model advances in the national centers for environmental Prediction operational mesoscale Eta model. *J. Geophys. Res.* **108** (2003).

96. Z. L. Yang *et al.*, The community Noah land surface model with multiparameterization options (Noah-MP): 2. Evaluation over global river basins. *J. Geophys. Res.* **116** (2011).
97. X. Cai *et al.*, Hydrological evaluation of the Noah-MP land surface model for the Mississippi River Basin. *J. Geophys. Res. Atmos.* **119**, 23–38 (2014).
98. J. Li *et al.*, Global evaluation of the Noah-MP land surface model and suggestions for selecting parameterization schemes. *J. Geophys. Res. Atmos.* **127**, e2021JD035753 (2022).
99. G. J. Huffman *et al.*, NASA global precipitation measurement (GPM) integrated multi-satellite retrievals for GPM (IMERG). Algorithm Theoretical Basis Document (ATBD). Version 4, 26 (2015).
100. R. Gelaro *et al.*, The modern-era retrospective analysis for research and applications, version 2 (MERRA-2). *J. Clim.* **30**, 5419–5454 (2017).
101. M. A. Friedl *et al.*, MODIS collection 5 global land cover: Algorithm refinements and characterization of new datasets. *Remote Sens. Environ.* **114**, 168–182 (2010).
102. T. Hengl *et al.*, SoilGrids250m: Global gridded soil information based on machine learning. *PLoS ONE* **12**, e0169748 (2017).
103. D. Yamazaki *et al.*, A high-accuracy map of global terrain elevations. *Geophys. Res. Lett.* **44**, 5844–5853 (2017).
104. R. E. Dickinson *et al.*, Interactive canopies for a climate model. *J. Clim.* **11**, 2823–2836 (1998).
105. J. T. Ball, I. E. Woodrow, J. A. Berry "A model predicting stomatal conductance and its contribution to the control of photosynthesis under different environmental conditions" in *Progress in photosynthesis research: volume 4 proceedings of the Vllth international congress on photosynthesis providence, Rhode Island, USA, august 10–15, 1986* (Dordrecht: Springer Netherlands, 1987), pp. 221–224.
106. G. J. Collatz, J. T. Ball, C. Grivet, J. A. Berry, Physiological and environmental regulation of stomatal conductance, photosynthesis and transpiration: A model that includes a laminar boundary layer. *Agric. For. Meteorol.* **54**, 107–136 (1991).
107. G. B. Bonan, Land surface model (LSM version 1.0) for ecological, hydrological, and atmospheric studies: Technical description and users guide. Technical note (No. PB-97-131494/XAB; NCAR/TN-417-STR). (National Center for Atmospheric Research, Climate and Global Dynamics Div., Boulder, CO, United States, 1996).
108. B. F. Zaitchik, M. Rodell, R. H. Reichle, Assimilation of GRACE terrestrial water storage data into a land surface model: Results for the Mississippi River basin. *J. Hydrometeorol.* **9**, 535–548 (2008).
109. R. H. Reichle, D. B. McLaughlin, D. Entekhabi, Hydrologic data assimilation with the ensemble Kalman filter. *Mon. Weather Rev.* **130**, 103–114 (2002).
110. R. H. Reichle *et al.*, Comparison and assimilation of global soil moisture retrievals from the Advanced Microwave Scanning Radiometer for the Earth Observing System (AMSR-E) and the Scanning Multichannel Microwave Radiometer (SMMR). *J. Geophys. Res.* **112** (2007).
111. W. T. Crow, M. J. Van den Berg, An improved approach for estimating observation and model error parameters in soil moisture data assimilation. *Water Resour. Res.* **46** (2010).
112. C. Draper, R. H. Reichle, Assimilation of satellite soil moisture for improved atmospheric reanalyses. *Mon. Weather Rev.* **147**, 2163–2188 (2019).
113. M. Giroto, R. Reichle, M. Rodell, V. Maggioni, Data assimilation of terrestrial water storage observations to estimate precipitation fluxes: A synthetic experiment. *Remote Sens.* **13**, 1223 (2021).
114. S. Boussetta *et al.*, Assimilation of surface albedo and vegetation states from satellite observations and their impact on numerical weather prediction. *Remote Sens. Environ.* **163**, 111–126 (2015).
115. R. H. Reichle *et al.*, Connecting satellite observations with water cycle variables through land data assimilation: Examples using the NASA GEOS-5 LDAS. *Surv. Geophys.* **35**, 577–606 (2014).
116. W. Nie *et al.*, Assimilation of remotely sensed leaf area index enhances the estimation of anthropogenic irrigation water use. *J. Adv. Model. Earth Syst.* **14**, e2022MS003040 (2022).
117. S. V. Kumar *et al.*, Assimilation of remotely sensed soil moisture and snow depth retrievals for drought estimation. *J. Hydrometeorol.* **15**, 2446–2469 (2014).
118. Q. Wen *et al.*, RobustSTL: A robust seasonal-trend decomposition algorithm for long time series. *Computer Sci.* **33**, 5409–5416 (2019).
119. R. B. Cleveland, W. S. Cleveland, J. E. McRae, I. Terpenning, STL: A seasonal-trend decomposition. *J. Off. Stat.* **6**, 3–73 (1990).
120. R. O. Gilbert, *Statistical Methods for Environmental Pollution Monitoring* (John Wiley & Sons, Inc., 1987).
121. C. Wasko, R. Nathan, M. C. Peel, Trends in global flood and streamflow timing based on local water year. *Water Resour. Res.* **56**, e2020WR027233 (2020).
122. B. Raup *et al.*, The GLIMS geospatial glacier database: A new tool for studying glacier change. *Glob. Planet. Change* **56**, 101–110 (2007).
123. W. N. Nie *et al.*, Data associated with the publication: Nonstationarity in the global terrestrial water cycle and its interlinkages in the Anthropocene. Johns Hopkins Libraries. <https://doi.org/10.7281/T1/KOTDPY>. Deposited 30 August 2024.